ChemPubSoc Europe

DOI: 10.1002/cctc.201500710

CHEMCATCHEM Full Papers

X-ray Fluorescence Tomography of Aged Fluid-Catalytic-Cracking Catalyst Particles Reveals Insight into Metal Deposition Processes

Sam Kalirai,[a] Ulrike Boesenberg,[b] Gerald Falkenberg,[b] Florian Meirer,*[a] and Bert M. Weckhuysen*[a]

Microprobe X-ray fluorescence tomography was used to investigate metal poison deposition in individual, intact and industrially deactivated fluid catalytic cracking (FCC) particles at two differing catalytic life-stages. 3D multi-element imaging, at submicron resolution was achieved by using a large-array Maia fluorescence detector. Our results show that Fe, Ni and Ca have significant concentration at the exterior of the FCC catalyst particle and are highly co-localized. As concentrations increase as a function of catalytic life-stage, the deposition profiles of Fe, Ni, and Ca do not change significantly. V has been shown to penetrate deeper into the particle with increasing catalytic age. Although it has been previously suggested that V is responsible for damaging the zeolite components of FCC particles, no spatial correlation was found for V and La, which was used as a marker for the embedded zeolite domains. This suggests that although V is known to be detrimental to zeolites in FCC particles, a preferential interaction does not exist between the two.

Introduction

Fluid catalytic cracking (FCC) catalysts are a major class of petrochemical catalysts that account for a significant portion of global gasoline production. In the FCC process, catalyst particles ranging in size from 50–150 μm are used to crack heavy crude oil fractions into lighter, more valuable hydrocarbons, such as gasoline. FCC particles are partially composed of active alumina and zeolite phases that perform the precracking and cracking, respectively.[1–3]

As the catalyst ages, the harsh physical and chemical process conditions cause a decline in the overall cracking capability of FCC catalyst particles. During cracking, these harsh conditions, in combination with contaminants present in the feedstock can cause irreversible physical and chemical damage to the particle.[4,5] Steaming and subsequent catalyst regeneration of FCC catalyst particles is performed after each cracking phase to combat reversible deactivation effects, such as coking.[6] However, the limited hydrothermal stability of zeolites make them susceptible to degradation under the harsh conditions of steaming and regeneration thereby diminishing the effective catalytic properties of the particle as a whole.[7–9] Owing to its superior hydrothermal stability, a mesoporous, dealuminated, zeolite Y (that is, Ultrastable Y, USY) is commonly utilized for FCC particles.[10] Furthermore, rare-earth (RE) metals, often La, are incorporated into USY to achieve even greater stability and increase the zeolite acid strength.[11,12]

In addition to zeolite deactivation through harsh hydrothermal conditions experienced by the catalyst, heavy oil fractions containing significant concentrations of Fe, Ni, V, Na, and Ca can trigger the irreversible deactivation of FCC catalyst particles. Fe, Ni, and V, are known to promote the formation of coke when they are incorporated into the FCC catalyst particle.[13,14] Furthermore, it has been proposed that these metals can cause accessibility loss by pore blocking[15] and chemically degrade the zeolite, consequently diminishing the cracking capability of the FCC catalyst.[16] Recently, it has been shown with X-ray tomography that Fe and Ni can cause severe pore clogging at the macroporous scale, thereby significantly altering the pore structure and resulting in a lower accessibility of the particle interior[17] with the effect becoming increasingly deleterious as a function of catalytic age.[18] Ni and V are known to promote dehydrogenation reactions, resulting in the promotion of coke formation and subsequent reduction in the yield of desired products.[19] Furthermore, V is believed to irreversibly degrade zeolite domains and cause destruction of the crystalline zeolite structure in FCC catalysts via the damaging effects arising from the formation of vanadic acid.[20,21]

[a] S. Kalirai, Dr. F. Meirer, Prof. Dr. B. M. Weckhuysen
Inorganic Chemistry and Catalysis Group
Debye Institute for Nanomaterials Science
Utrecht University
Universiteitsweg 99, 3584 CG, Utrecht (The Netherlands)
E-mail: f.meirer@uu.nl
b.m.weckhuysen@uu.nl

[b] Dr. U. Boesenberg, Dr. G. Falkenberg
Deutsches Elektronen-Synchrotron DESY
Notkestrasse 85, 22607 Hamburg (Germany)

Supporting Information for this article is available on the WWW under http://dx.doi.org/10.1002/tc.2.201500710.

Part of a Special Issue on Advanced Microscopy and Spectroscopy for Catalysis. A link to the Table of Contents will appear here once the Special Issue is assembled.

Thus, the study of the deposition and distribution of Fe, Ni, and V are of critical importance for understanding FCC deactivation and ultimately, the design of more robust cracking catalysts. Previous studies have been focused towards studying either the bulk effects of Fe, Ni, and V on catalyst samples,[15,22] and/or investigating artificially metalated single catalyst particles to simulate metal-induced deactivation phenomena.[23,24] Recently, there has been an effort to understand catalytic phenomena at the single particle level by utilizing synchrotron-based X-ray imaging techniques in the field of heterogeneous catalysis.[25–30] In their elegant study, Bare et al. have shown the ability to map void structures with a voxel size of approximately 40 nm for a subsection of an authentic FCC particle using 3D X-ray tomography.[31] They also used 2D X-ray fluorescence (XRF) imaging to map elemental distributions of metal poisons, such as Fe, Ni, and V, as well as structural components, such as the clay and zeolite domains.[31] Da Silva et al. were able to determine the pore size distribution for a particle subsection with high spatial resolution using ptychographic X-ray tomography on a model FCC composite-catalyst particle system.[32] However, despite these fundamental insights into the pore structure of FCC catalyst particles, relatively little progress has been made to measure the effects metals have on the pore structure.

Our group has recently made efforts to understand FCC catalyst particle pore structure and the changes imparted on to it by the deposition of Fe and Ni using synchrotron-based X-ray nanotomography.[17,18] It was shown that the metals accumulate at the periphery of the FCC catalyst particle and significantly decrease the porosity, which in turn affects accessibility of the particle as a whole. As a catalyst ages, this blocking can become so severe that pore networks effectively segregate into a series of isolated subnetworks as a result of the metal blockage.[18] Furthermore, an excess buildup of metals may also result in the agglomeration of FCC catalyst particles, thereby diverting the FCC catalyst from its primary function.[33] However, these studies were unable to probe the distribution of V as well as structural components such as La and Ti. This is, in part due to the large number and diverse energy ranges required to map all relevant elements, and in part due to the low concentrations of certain metals, specifically V, in relevant (that is, not artificially metalated by Mitchell impregnation) FCC catalysts, which can fall below the detection limits of X-ray transmission measurements. Furthermore, elements such as Ca, La, V, and Ti can be difficult to accurately measure in full-field experiments because of the low edge energy at which there is a notably low photon flux owing to X-ray attenuation in air. Furthermore, our group has performed XRF experiments simultaneously with X-ray diffraction (XRD) and X-ray absorption measurements to understand the effects of V and Ni, which were detected by XRF, with respect to the zeolite domains, which were localized by XRD.[34] Although the general V and Ni distributions were determined by XRF, the XRF maps suffered from self-absorption effects resulting from the thickness of the particle, and single detector scheme, thus an accurate picture of the distribution was difficult to determine.

Despite the difficulties surrounding XRF measurements, the elemental sensitivity and simultaneous detection of multiple elements makes synchrotron based XRF an ideal technique for the analysis of single catalyst particles[35,36] particularly at industrially relevant metal (poison) concentrations, as is the case for FCC catalyst particles.[37] In comparison to X-ray transmission experiments, XRF tomography provides simultaneous detection of multiple elements of interest at a higher sensitivity. However, up to this point, XRF tomographic studies of catalyst particles have been limited by the spatial resolution that is typically achievable by microbeam XRF techniques (typical beam sizes are in the single micrometer range), the experimental time needed to scan large sample volumes (most often $>1000\ \mu m^3$) with beam sizes smaller than 1 μm, and complications due to self-absorption effects. These limitations have recently been tackled by the use of powerful X-ray optics and large array, high count rate detectors, thus making XRF tomography in the sub-micron voxel regime technically feasible with measurement times comparable to that of sub-100 nm synchrotron-based tomography techniques.

In this study, we have used multielement XRF tomography with the large array Maia detector, as illustrated in Figure 1, to investigate the 3D distributions of structural and deposited elements in genuine, industrial FCC catalyst particles. Measurements have been performed on two industrially deactivated FCC catalyst particles—the life stage of which has been deter-

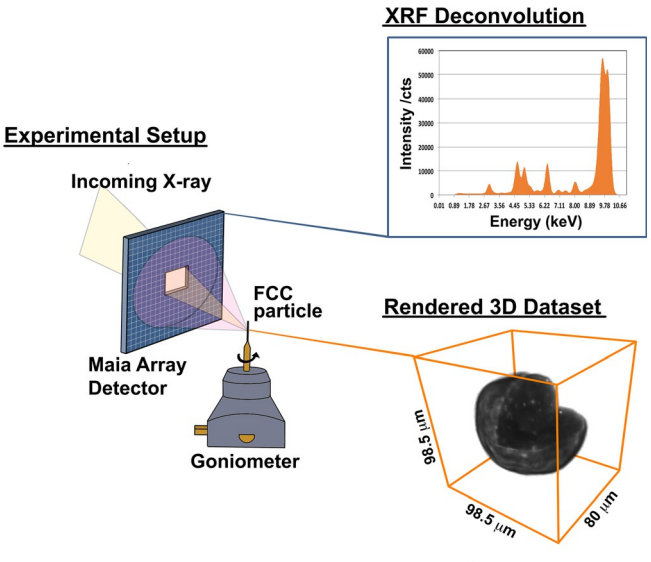

Figure 1. Experimental setup and detection scheme. Left) The experimental setup uses KB focusing optics to focus X-rays to a 500 nm spot where the sample sits on a goniometer. The sample is raster-scanned to build up the image and may be rotated to collect projection images at multiple angles for tomography studies. The Maia detector is used to detect the outgoing fluorescence at a large solid angle in a back-scattering geometry. Top right) First the XRF spectrum of the whole FCC catalyst particle is evaluated using dynamic analysis to obtain the individual elemental signatures. This deconvolution of the XRF data is then performed for all single-pixel spectra and all projection images to provide elemental maps at each angle. Bottom right) In the final step all elemental maps are aligned and reconstructed to obtain the 3D distribution of each element. The panel shows a representation of the whole ECAT2 particle using the sum of all elemental channels.

mined by the relative metals content present—focusing on the poisonous metals Fe, Ni, Ca, V, their distribution amongst the particles, and their potential correlation with zeolite domains. The two catalyst particles will be further referred to as ECAT1 and ECAT2. The results show that during the FCC particles catalytic life the concentrations of the poisonous metals Fe, Ni, Ca, and V increase with age and also that the different mobility of each element leads to observable differences in their 3D distribution. Correlation analysis shows that Fe, Ni and Ca have similar deposition profiles, where the majority of the metals are present at the exterior of the FCC catalyst particle. In contrast, V exhibits a larger penetration depth into the particle and is less correlated to the other metals, therefore suggesting differences in the metal deposition mechanisms of V with respect to the other metal poisons.

Results and Discussion

In Figure 1 the experimental setup, including the information gathered from the measurements used, is shown schematically. The Maia detector is used to collect an XRF spectrum at each pixel. The XRF spectra were deconvoluted using the GeoPIXE analysis software.[38] The deconvolution was performed for every single pixel in order to obtain 2D maps of all detected elements (Figure 1, XRF spectrum). This measurement/analysis scheme simultaneously provides information on a diverse range of elements at ms dwell times. The sample can be rotated to collect maps at different angles and thereby obtaining 3D information through tomographic reconstruction for all elements observed in the XRF spectra (Figure 1, rendered 3D dataset). Owing to the small single-pixel dwell times, XRF tomography data are collected in 8–10 h.

In Figure 2, the summed XRF spectrum over the whole catalyst particle is shown for a single projection image of ECAT1 and ECAT2 FCC catalyst particle, respectively. After background correction and based on the identified XRF peaks, spectra were fitted using a fitting model including Ca, Ti, La, V, Cr, Fe, Ni, Cu, Zn elemental channels as well as contributions from elastic and inelastic scattering. In this study experimental conditions were optimized for the detection of the metal poisons Fe, Ni, V, Ca, as well as elements related to structural components, that is, La and Ti. Cu and Zn were detected and therefore included in the fitting model, but not further investigated because of the overlap with the scatter peaks.

In Table 1, the relative elemental concentrations of Fe, Ni, V, Ca, La, and Ti over the individual FCC catalyst particles are shown. The relative concentrations were determined by normalizing the integrated peak intensity for each individual elemental channel to the summed intensity over all element channels. It can be seen that there is an increase in the relative elemental percentage of poisonous metals Fe, Ni, V, and Ca from ECAT1 to ECAT2. In both FCC catalyst particles, the amount of Fe is the largest, as it is present in both the matrix and deposited as a poison. La has the second largest relative concentration because it is present in the RE-exchanged zeolite domains distributed throughout the FCC catalyst particle. The relative decrease in the amount of La of ECAT2 compared

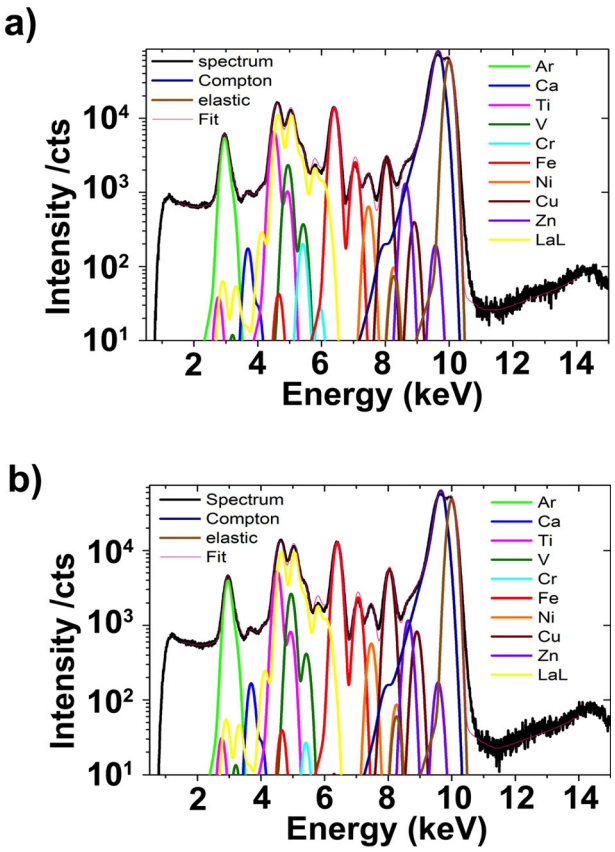

Figure 2. XRF spectrum deconvolution of the single FCC catalyst particles: a) ECAT1 and b) ECAT2. The spectra are the sum over the whole particle at a single projection image. From this the presence of Ca, Ti, V, Cr, Fe, Ni, Cu, Zn, and La was confirmed. Each single-pixel XRF spectrum was then fitted using GeoPIXE providing peak areas for each individual element.

Table 1. Relative elemental concentrations for the ECAT1 and ECAT2 FCC catalyst particles under study.

Element	ECAT1 [%]	ECAT2 [%]
Fe	41.92	44.18
Ni	2.38	3.34
V	2.62	4.84
Ca	1.25	1.35
La	35.10	31.38
Ti	16.73	14.91

to ECAT1 suggests that there is an increased deposition of metals. The amounts of Ni and V are significantly lower than the amount of Fe, as they are only present as contaminants in the FCC catalyst particle, and thus are only deposited on the particle during cracking. As Ni is not inherently present in the fresh catalyst, its amount is directly related to the amount of Ni present in the feedstock. Thus, as previously suggested, Ni was used to classify the particles based upon their catalytic age.[39] It was determined that ECAT1 is catalytically „younger" than ECAT2. With this age classification method, these two catalyst particles can then be used to gain insight into possible temporal changes of metal deposition.

The poisonous metals Fe, Ni, V, and Ca, as well as the structural component La have been further investigated with respect to their 3D radial distribution within the catalyst particles to understand metal deposition in the particles. To quantify the radial dependence of the relative elemental concentrations over the total particle volume we have calculated them as a function of distance from the surface (Supporting Information). The result of this effort is summarized in Figure 3 for ECAT1 and ECAT2, respectively. The cumulative intensity of each of the metal poisons was determined as a function of distance of each "particle shell" from the surface, for which each shell is formed by all voxels with identical distance to the surface. This shell analysis provides insight into the distribution of metals and their depth of penetration.[17]

For both ECAT1 and ECAT2, the amount of Fe shows a peak at 0.5–1 μm from the surface. The peak Ni and Ca amounts for both ECAT1 and ECAT2 catalyst particles also occur at 0.5–1 μm distance from the surface but at a lower relative concentration (Figure 3, inset). From the high-concentration peak at the surface both Fe, Ni, and Ca concentrations fall with increasing distance from the particle surface. Fe shows a constant, nonzero intensity inside the particle, caused by the presence of Fe in the structural components, such as in the matrix. The peak Fe intensity falls to the distinct baseline level seen in the matrix of both ECAT1 and ECAT2 particle within 5 μm from the surface, thus showing that the two particles appear to be indistinct in the particle interior. The Ni and Ca concentrations fall to undetectable amounts slightly deeper than 5 μm distance from the catalyst particle surface. It is seen that the intrusion of Fe, Ni, and Ca does not change significantly as a function of age; however, as the catalyst ages, an accumulation of the metals at or near the surface of the particle occurs. Previous studies have stated that Fe and Ni have limited mobility in FCC catalyst particles, and, particularly for Fe, the formation of a hard, nodulated crust around the particle surface may be observed.[40–42] This concentration at the surface can cause significant pore blockage at the exterior of the surface, and in effect may prevent both metal poisons and the hydrocarbon feedstock from penetrating into the particle interior.[18]

V exhibits a peak concentration that is different from that of Fe and Ni. The V peak appears at approximately 1.5–2 μm distance from the surface and then falls to undetectable levels at slightly larger distances from the surface than Ni and Ca. In the ECAT1 particle, the amount of V falls to zero at approximately 5 μm from the sample. However, in the ECAT2 particle V exhibits observable intensity until approximately 9 μm deep into the sample. This is in agreement with previous assertions that V mobility is higher than Fe or Ni in FCC.[20,43] The difference in the deposition and migration of V with respect to nonmobile metals may be related to the transportation of V through the vapor phase present during hydrothermal conditions.[43] This observation further suggests that as the particle ages, the accumulation of V increases, and owing to its higher mobility, is able to access pore space deeper into the particle with appreciable concentrations despite pore blockage occurring from Fe and Ni. However, there remains a concentration gradient with a peak near the catalyst particle surface and minimum at the center of the particle, as seen in the study by Ruiz-Martinez et al.[34] This observation is contrary to other reports that show that V can be distributed more homogeneously in the particle.[31,44]

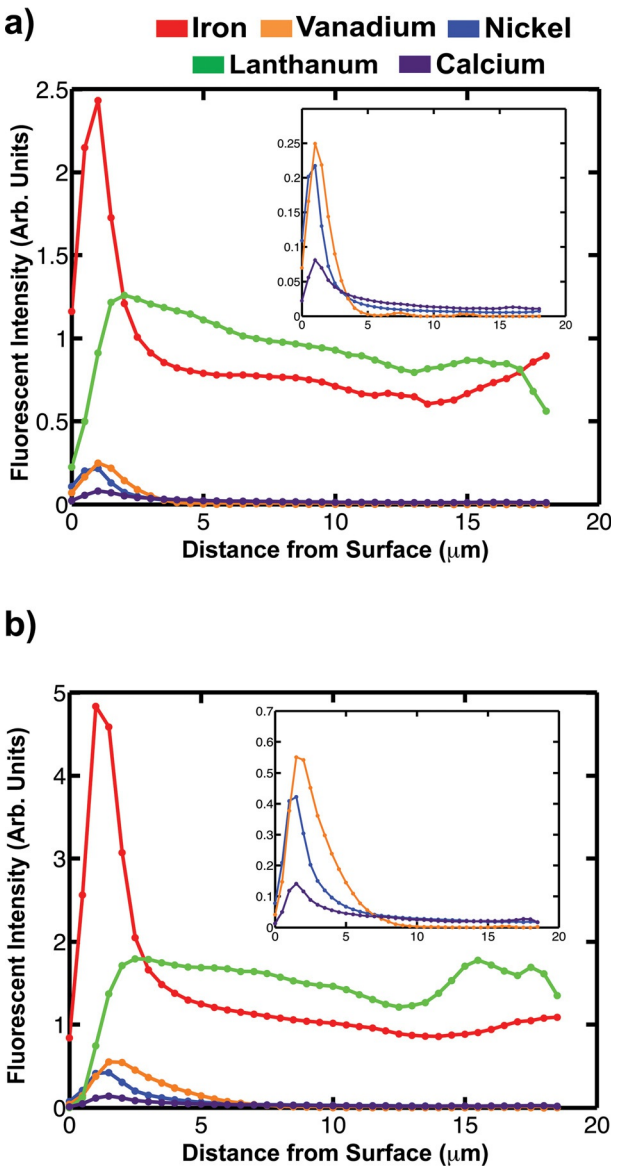

Figure 3. Distribution of relative elemental concentrations for iron, nickel, vanadium, lanthanum, and calcium as a function of distance from the surface for a) the ECAT1 FCC catalyst particle and b) the ECAT2 FCC catalyst particle. The insets give an enlargement of the peak intensities for V, Ni, and Ca.

These observed differences in the distribution of mobile species, such as V, may result from the effect of the nonmobile metals deposited on the FCC catalyst particles. In previous studies, in which a uniform distribution of V was exhibited, the distribution of Fe was seen to be nonuniform on the surface[31] or not studied.[44] However, in this study, we observed that the Fe distribution was present uniformly (Figure 4), at high concentrations, along the exterior of the particle, thus possibly limiting accessibility by blocking up a significant portion of the potential intrusion pathways for V. This suggests that the

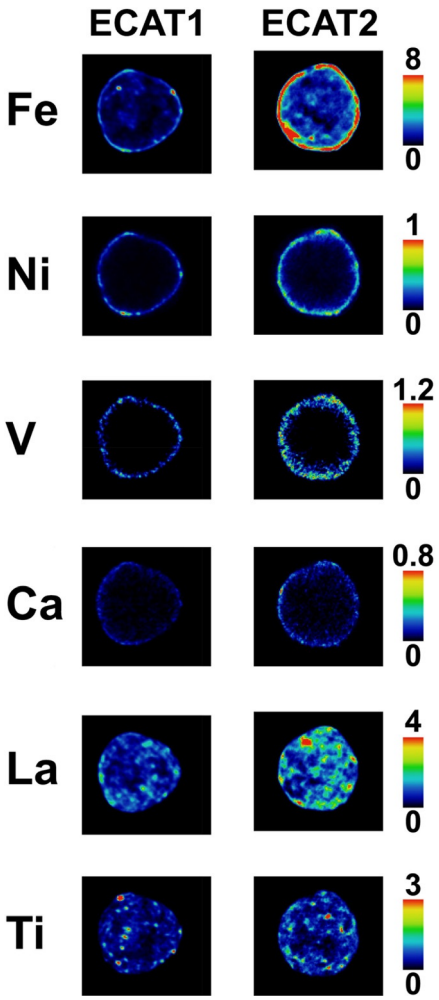

Figure 4. 2D slices for each elemental channel of the 3D ECAT1 and ECAT2 FCC catalyst particles. The scale bars indicate the intensity limits set to the same values for both ECAT1 and ECAT2.

metal deposition profiles can vary greatly based upon the conditions experienced in the feedstock and the order in which they were experienced. This can lead to a large variation in V deposition profiles as evidenced by 2D XRF elemental maps (Supporting Information) of ECAT FCC catalyst thin-section samples that clearly exhibit diverse ranges of V distributions, from homogeneous to radially dependent distributions as seen in the 3D data.

In both the ECAT1 and ECAT2 FCC catalyst particles, the La channel shows a nearly constant intensity from the particle exterior to the center, signifying that there is a relatively homogeneous distribution of zeolite domains throughout the particle. Furthermore, it shows that self-absorption effects have been minimized by collecting full 360° projections images and by the use of the large array detector, which provides a large solid angle and thus a large number of escape paths. Self-absorption effects can arise from fluorescence attenuation by the catalyst particle. This attenuation is stronger at lower energies where X-ray absorption cross-sections are high. By performing a full 360° redundant tomographic data collection scheme, one is able to identify self-absorption. It may be argued that owing to the low fluorescence energy and low concentration of V the radial profile observed is primarily the result of self-absorption effects in conjunction with the use of 360° data collection. However, we have shown that the elemental distribution remains basically unchanged if reconstruction is performed with two half datasets (that is, 0–180° and 181–360°), in which self-absorption effects, if present, would be significantly increased and become clearly visible (Supporting Information).

In Figure 4 2D slices taken from the 3D datasets at each elemental channel are shown. To compare the relative intensity, the intensity scale bars were set to equal ranges for both the ECAT1 and ECAT2 FCC catalyst particles. It can be clearly seen that Fe deposited on the surface exhibits a uniform distribution of high intensity at the exterior of the particle, in line with the radial profiles observed. However, for the ECAT1 catalyst, although there is a clear ring of high intensity, there are still low-intensity regions that exist. These regions are likely the "highways" that allow for V to intrude further in to the particle as it catalytically ages. However, if the pathways are quickly closed up, owing to the presence of a high concentration of Fe in the feedstock, the accessibility of the particle interior is extremely diminished and a uniform distribution of V is unlikely to occur because of the surface clogging effects. It can be observed in the Ni 2D map that the distribution, particularly that in the ECAT1 particle, is closely correlated with that of Fe. Some of the Fe hot-spot regions on the surface of the particles are mirrored for Ni suggesting that there is a correlated deposition mechanism for the two metals. In the V map, the correlation to Fe is questionable, as there are no real hot spots observed such as those in Fe and Ni, however, there is some correspondence of high intensity at the bottom and the top of the particle. In comparing the ECAT1 and the ECAT2 FCC catalyst particles, it can be clearly seen that V has penetrated deeper in to the particle as the particle has aged, as signified by the radial maps in Figure 3. Ti and La remain relatively unchanged, with a uniform distribution throughout the particle from ECAT1 to ECAT2.

To investigate these correlations in the spatial distribution of elements, correlation plots for each of the elements of interest were created. In Figure 5, the correlation heat maps for all bivariate combinations between the elements Fe, Ni, V, Ca, La, and Ti are shown for the ECAT1 and ECAT2 FCC catalyst particles. Furthermore, the Pearson correlation coefficient of each of the element pair combinations for the ECAT1 and ECAT2 catalyst particles were calculated and are shown for each combination in the upper right half of Figure 5a and b and summarized in Figure 5c. The Pearson correlation coefficients were calculated after removing values under the calculated threshold for each elemental channel and the null (0,0) results to remove voxels without any element present, which can skew the correlation results by their predominance.

Fe and Ni exhibit a high spatial correlation. The correlation coefficient for Fe and Ni was determined to be 0.728 for ECAT1 and 0.870 for ECAT2. The higher correlation in the ECAT2 particle is presumed caused by Fe and Ni present in the outer shells of the particle. However, as Fe is also present in

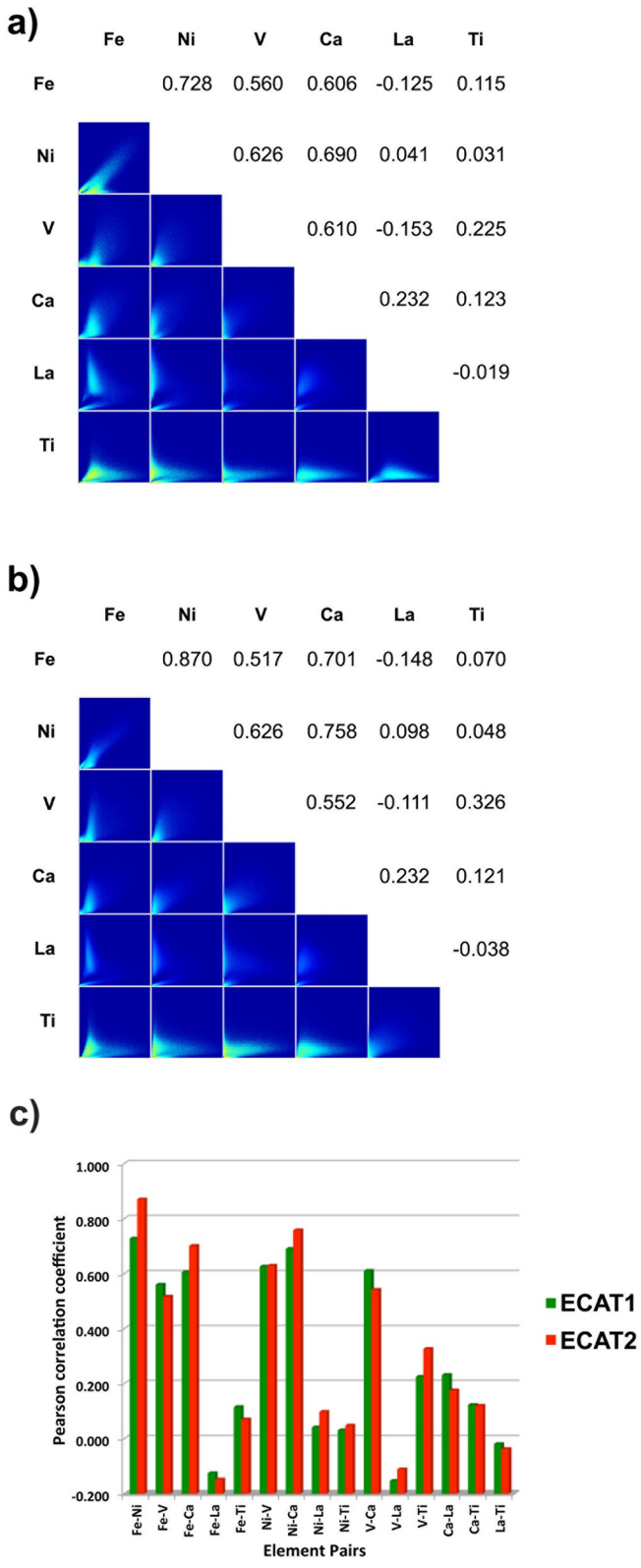

Figure 5. Spatial correlation heat maps matrix for all elemental combinations of the a) ECAT1 and b) ECAT2 FCC catalyst particles for pixels within 95% of the maximum (to remove outliers). c) Bar plot of the Pearson correlation coefficients for all element pair combinations for ECAT1 and ECAT2 FCC catalyst particles.

the matrix, and thus in the interior of the particle, it is expected that the Fe and Ni correlation is less if the amount of deposited Fe on the exterior is lower (in ECAT1), because Ni is only deposited on the FCC particle and was shown to be largely present at the particle edges. The Fe/Ca and Ni/Ca combinations also show a high correlation, that is, ECAT1 0.606, 0.690 and ECAT2 0.701, 0.758, respectively. Yaluris et al. have shown that Fe and Ca have similar distribution profiles and may be correlated on the surface of the particle.[42] It has been previously suggested that Ca and Fe combine to form a vitrified layer on the catalyst exterior. In addition, Ca can further reduce the catalytic activity by making the FCC particle more susceptible to hydrothermal deactivation.[45] The Fe–La, Ni–La, and V–La correlations remain relatively constant from ECAT1 to ECAT2 and are all close to zero (that is, are not correlated), mainly because the metals do not intrude far enough into the catalyst particle interior to associate with La-rich zones.

Some studies have attempted to understand V deposition with respect to the zeolite domains, however, the preference of V towards zeolite has remained unclear. Both studies from Kugler and Leta.[41] and Psarras et al.[22] observed a uniform distribution of V throughout an individual catalyst particle with some indication of preferential residence in zeolite domains. Other studies, such as Ruiz-Martinez et al.[34] and Lappas et al.[44] observed a ring-like intensity profile of V without clear preference for zeolite domains. In this study, the correlation of V to the zeolite domains was not observed in the FCC catalyst particles despite the intrusion of V into the particle (Figures 3 and 4). V does exhibit a slightly larger correlation to Ti (ECAT1 0.225, ECAT2 0.326) signifying that if there is any preferential residence of V, it is with the other components present in the FCC particle. However, at such low correlation coefficients, it is difficult to ascertain a preference of V within the FCC catalyst particle. In FCC catalyst design, the matrix can be used as a metal trap for V.[20] If V is causing the direct degradation of zeolite domains, it must be occurring at either low concentration and/or transiently, during steaming. V has been postulated to promote the degradation of zeolite domains when it is present as a vanadic acid species that is formed during steaming, thus it is possible that a preference of V towards the zeolite exists in its acidic form; a form which was not observed in this study as the experiments were performed under ambient conditions.[20]

The correlation plots in Figure 5a and b were manually clustered into quadrants, and segmented (Supporting Information) to visualize the distribution of metal poison elements that are both co-localized and independently located. Inspection of the correlation plots showed that some clustering of the data existed for the Fe–Ni, Fe–V, and Fe–Ca pairs, suggesting that there are distinct regions with differing relative elemental concentrations. The four clusters were masked, mapped back into 3D and visualized. In Figure 6, the clustered masks over the 3D representation of the FCC catalyst particles are shown for Fe with Ni, V, and Ca, respectively.

Fe and Ni demonstrate a correlation on the outer shell of the ECAT1 and ECAT2 catalyst particles, with little change as a function of age, suggesting that there is no redistribution of

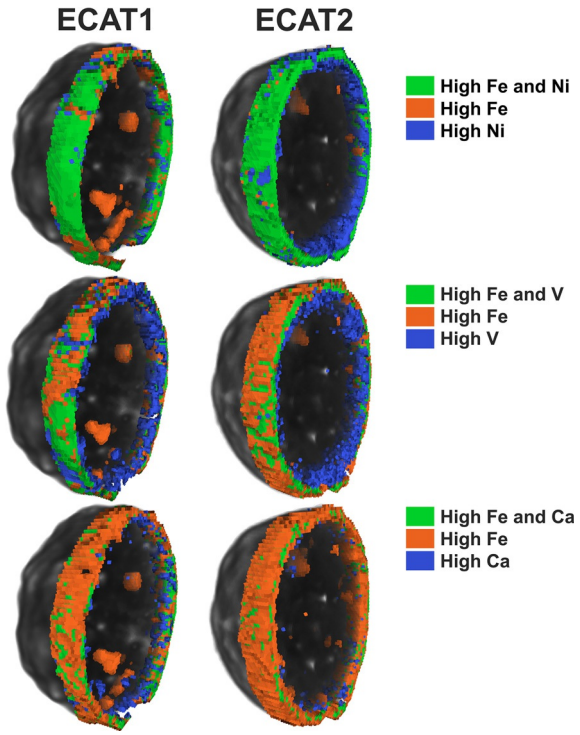

Figure 6. Comparison of clustering masks for a) ECAT1 and b) ECAT2 FCC catalyst particles for the correlation pairs Fe/Ni (top), Fe/V (middle) and Fe/Ca (bottom).

either metal but only an increase in surface concentration as the particle ages. Furthermore, hotspots of high Fe without Ni are present in the interior of the particle, which are interpreted as hotspots inherent to the clay components of the catalyst. By comparing Fe and V it is seen that in the ECAT1 catalyst particle the correlated Fe and V exists sparsely near the surface. Although Fe and V are correlated at the exterior of the particle, Fe is also visible without the presence of V at the edges of the particle. In the ECAT2 catalyst particle the co-localization is more uniform on the particle surface and also somewhat into the interior of the particle in which V has deposited deeper into the catalyst body suggesting further that the deposited, immobile Fe may contribute to a loss in mobility for V. With respect to Ca, there is some overlap between Fe and Ca for both catalyst particles and Ca does not appear independently from Fe. The Fe in the matrix shows little correlation with Ca. These observations suggest that V is indeed more closely incorporated into the existing particle structure, whereas Fe, Ca, and Ni all seem to be largely correlated at or outside the boundaries of the FCC catalyst particle.

Conclusions

We have shown that X-ray fluorescence (XRF) tomography of genuine, whole individual fluid catalyst particle is possible using the Maia detector setup at the P06 beamline at the Petra III lightsource (DESY, Hamburg, Germany). This unique setup allows for the collection of XRF tomographic data for a large range of elements at comparable experimental times to that of single energy tomographic measurements using X-ray transmission imaging techniques,[17,18,33] albeit still at a lower spatial resolution. In the future, this method may be used to complement high-resolution techniques to study both the elemental distributions as well as pore structure, and pore-size distribution on individual catalyst particles.

The conducted XRF tomography study on the catalytically younger catalyst, ECAT1, and the older ECAT2 catalyst has provided invaluable insight into their 3D metal distribution, particularly for V and Ni, which are typically present at low concentrations in FCC particles that have experienced industrial conditions. It was shown that for all poisonous metals, specific to the particles under study, there is a radial concentration gradient in which the concentration goes from a maximum near the surface of the catalyst particle to the interior. Surprisingly, V is not uniformly distributed in the particle as previously observed. We hypothesize that differences in the observed deposition of the mobile metal species are responsible for the distribution, for example, V may be dependent on the presence and distribution of nonmobile metals, such as Fe, Ni, and Ca, which can significantly alter the particle accessibility[18] and thus the 3D distribution of the mobile poisonous metals. Such a study on the distribution of V in 3D and insights into the dynamics of the distribution has not previously been reported in the literature. Furthermore, most studies have focused exclusively on one of the three main metal poisons, Fe, Ni, and V with little attention to the synergistic effects of these metals despite the significant impact on some metals to the pore structure[18] and thus the effect on the deposition schemes of other metals.

By inspecting the correlation of the metal poisons it was shown that Fe, Ni, and Ca are highly correlated, particularly at the surface of the particle where they form a shell around the catalyst particle. This suggests that these three elements have similar deposition mechanisms. Ni and especially V penetrate further into the catalyst particle, whereas Fe only appears as hotspots within the catalyst particle. These Fe concentrations in the interior parts of the particle are not deposited during catalyst aging but belong to Fe-rich matrix components of the catalyst particle. V has the greatest penetration depth into the FCC catalyst particle. This depth increases significantly as a function of catalyst age. This suggests that there is a different deposition and migration mechanism for V, in line with the differences in mobility compared to Fe, Ni, and Ca. Surprisingly, no spatial correlation of V with La has been observed, suggesting that V does not specifically interact with the embedded zeolite domains and is present near the matrix components of FCC catalyst particles, including alumina near which it may negatively impact the vital precracking functionality of the FCC catalyst particle.

Experimental Section

Fluid catalytic cracking particles

FCC catalyst particles were obtained from a full-scale, operational industrial reactor. FCC catalyst particles undergo significant deacti-

vation and those that are of a certain age are removed from the feed and replenished by new catalyst particles. This results in a broad age distribution for the catalysts in the feed. The term used for these catalysts with a broad age distribution is equilibrium catalyst or ECAT. The ECAT particles (labelled as ECAT1 and ECAT2) under study were selected randomly and age classified by their Ni metal content.[39]

Micro-X-ray fluorescence tomography

XRF tomography measurements were performed at the P06 beamline at the PETRA III synchrotron, DESY, Hamburg (Germany).[46] A monochromatic X-ray beam of 10.0 keV was focused to a 0.5× 0.5 μm^2 spot using KB-mirror optics. The sample was placed in the focal spot and raster scanned to make a point-by-point image. The energy-dispersed fluorescent signal was detected using a 384-element Maia detector array.[47] The Maia detector, with its large solid angle of acceptance allows for point dwell times on the millisecond timescale. The sample in the Kapton capillary was mounted on a goniometer and placed in the center of rotation. Projection images were collected at 1–1.5° angle steps for 360° full rotation to check for self-absorption effects (Supporting Information).

Data analysis

Fitting of the XRF spectra was performed by GeoPIXE software[38] by sampling the whole catalyst particle for a single projection image and determining the relevant XRF channels, which were then fitted at every pixel for every projection image. The resulting images for each channel were then aligned with imageJ software[48] and reconstructed using an iterative Algebraic Reconstruction Technique (i-ART) algorithm with TXM-Wizard.[49] 3D datasets were visualized using the Avizo Fire software and further analysis was performed using MATLAB.

Acknowledgements

This work is supported by the NWO Gravitation program, Netherlands Center for Multiscale Catalytic Energy Conversion (MCEC) and a European Research Council (ERC) Advanced Grant (321140). Parts of this research were carried out at the light source PETRA III at DESY, a member of the Helmholtz Association (HGF). We would like to thank Dr. Matthias Alfeld for assistance in using beamline P06. We would like to thank Dr. Wout de Nolf for helping with collecting and analyzing the 2D XRF data shown in the Supporting Information.

Keywords: cracking · X-ray fluorescence · lanthanum · vanadium · zeolites

[1] S. Al-Khattaf, *Appl. Catal. A* **2002**, *231*, 293 – 306.
[2] N. Hosseinpour, Y. Mortazavi, A. Bazyari, A. A. Khodadadi, *Fuel Process. Technol.* **2009**, *90*, 171 – 179.
[3] A. Corma, A. V. Orchillés, *Microporous Mesoporous Mater.* **2000**, *35 – 36*, 21 – 30.
[4] H. S. Cerqueira, G. Caeiro, L. Costa, F. Ramôa Ribeiro, *J. Mol. Catal. A* **2008**, *292*, 1 – 13.
[5] Q. L. Wang, G. Giannetto, M. Torrealba, G. Perot, C. Kappenstein, M. Guisnet, *J. Catal.* **1991**, *130*, 459 – 470.
[6] N. E. Lindsay, N. Park, *Geothermics* **1985**, *14*, 595 – 599.
[7] R. A. Beyerlein, C. Choi-feng, J. B. Hall, B. J. Huggins, G. J. Ray, *Top. Catal.* **1997**, *4*, 27 – 42.
[8] J. Scherzer, *Appl. Catal.* **1991**, *75*, 1 – 32.
[9] B. Xu, S. Bordiga, R. Prins, J. A. van Bokhoven, *Appl. Catal. A* **2007**, *333*, 245 – 253.
[10] J. García-Martínez, K. Li, G. Krishnaiah, *Chem. Commun.* **2012**, *48*, 11841 – 11843.
[11] E. F. Sousa-Aguiar, F. E. Trigueiro, F. M. Z. Zotin, *Catal. Today* **2013**, *218 – 219*, 115 – 122.
[12] R. Carvajal, *J. Catal.* **1990**, *125*, 123 – 131.
[13] E. Tangstad, A. Andersen, E. M. Myhrvold, T. Myrstad, *Appl. Catal. A* **2008**, *346*, 194 – 199.
[14] M. Xu, X. Liu, R. J. Madon, *J. Catal.* **2002**, *207*, 237 – 246.
[15] Z. Yuxia, D. Quansheng, L. Wei, T. Liwen, L. Jun, *Stud. Surf. Sci. Catal.* **2007**, *166*, 201 – 212.
[16] A. S. Escobar, F. V. Pinto, H. S. Cerqueira, M. M. Pereira, *Appl. Catal. A* **2006**, *315*, 68 – 73.
[17] F. Meirer, D. T. Morris, S. Kalirai, Y. Liu, J. C. Andrews, B. M. Weckhuysen, *J. Am. Chem. Soc.* **2015**, *137*, 102 – 105.
[18] F. Meirer, S. Kalirai, D. Morris, S. Soparawalla, Y. Liu, G. Mesu, J. C. Andrews, B. M. Weckhuysen, *Sci. Adv.* **2015**, *1*, e1400199.
[19] T. F. Petti, D. Tomczak, C. J. Pereira, W.-C. Cheng, *Appl. Catal. A* **1998**, *169*, 95 – 109.
[20] C. Trujillo, U. N. Uribe, P. Knops-Gerrits, L. A. Oviedo, P. A. Jacobs, *J. Catal.* **1997**, *168*, 1 – 15.
[21] R. F. Wormsbecher, *J. Catal.* **1986**, *100*, 130 – 137.
[22] A. C. Psarras, E. F. Iliopoulou, L. Nalbandian, A. A. Lappas, C. Pouwels, *Catal. Today* **2007**, *127*, 44 – 53.
[23] D. R. Rainer, E. Rautiainen, P. Imhof, *Appl. Catal. A* **2003**, *249*, 69 – 80.
[24] T. Myrstad, B. Seljestokken, H. Engan, E. Rytter, *Appl. Catal. A* **2000**, *192*, 299 – 305.
[25] A. M. Beale, S. D. M. Jacques, B. M. Weckhuysen, *Chem. Soc. Rev.* **2010**, *39*, 4656 – 4672.
[26] B. M. Weckhuysen, *Angew. Chem. Int. Ed.* **2009**, *48*, 4910 – 4943; *Angew. Chem.* **2009**, *121*, 5008 – 5043.
[27] A. M. Beale, S. D. M. Jacques, E. K. Gibson, M. Di Michiel, *Coord. Chem. Rev.* **2014**, *277 – 278*, 208 – 223.
[28] S. Bordiga, E. Groppo, G. Agostini, J. A. van Bokhoven, C. Lamberti, *Chem. Rev.* **2013**, *113*, 1736 – 850.
[29] J. D. Grunwaldt, C. G. Schroer, *Chem. Soc. Rev.* **2010**, *39*, 4741 – 4753.
[30] I. L. C. Buurmans, B. M. Weckhuysen, *Nat. Chem.* **2012**, *4*, 873 – 886.
[31] S. R. Bare, M. E. Charochak, S. D. Kelly, B. Lai, J. Wang, Y. K. Chen-Wiegart, *ChemCatChem* **2014**, *6*, 1427 – 1437.
[32] J. C. da Silva, K. Mader, M. Holler, D. Haberthür, A. Diaz, M. Guizar-Sicairos, W.-C. Cheng, Y. Shu, J. Raabe, A. Menzel et al., *ChemCatChem* **2015**, *7*, 413 – 416.
[33] F. Meirer, S. Kalirai, J. N. Weker, Y. Liu, J. C. Andrews, B. M. Weckhuysen, *Chem. Commun.* **2015**, *51*, 8097 – 8100.
[34] J. Ruiz-Martínez, A. M. Beale, U. Deka, M. G. O'Brien, P. D. Quinn, J. F. W. Mosselmans, B. M. Weckhuysen, *Angew. Chem. Int. Ed.* **2013**, *52*, 5983 – 5987; *Angew. Chem.* **2013**, *125*, 6099 – 6103.
[35] S. W. T. Price, K. Ignatyev, K. Geraki, M. Basham, J. Filik, N. T. Vo, P. T. Witte, A. M. Beale, J. F. W. Mosselmans, *Phys. Chem. Chem. Phys.* **2015**, *17*, 521 – 529.
[36] J. D. Grunwaldt, J. B. Wagner, R. E. Dunin-Borkowski, *ChemCatChem* **2013**, *5*, 62 – 80.
[37] F. Adams, K. Janssens, A. Snigirev, *J. Anal. At. Spectrom.* **1998**, *13*, 319 – 331.
[38] C. G. Ryan, D. R. Cousens, S. H. Sie, W. L. Griffin, *Nucl. Instrum. Methods Phys. Res. Sect. B* **1990**, *49*, 271 – 276.
[39] F. Hernández-Beltrán, E. López-Salinas, R. García de León, E. Mogica-Martínez, J. C. Moreno-Mayorga, González-Serrano in *Fluid Catalytic Cracking V Materials and Technological Innovations, Vol. 134* (Eds: M. L. Occelli, P. O'Connor), Elsevier, **2001**, pp. 87 – 106.
[40] O. Bayraktar, E. L. Kugler, *Catal. Lett.* **2003**, *90*, 155 – 160.
[41] E. Kugler, D. P. Leta, *J. Catal.* **1988**, *109*, 387 – 395.
[42] G. Yaluris, W.-C. Cheng, M. Peters, L. T. T. Mcdowell, L. Hunt in *Fluid Catalytic Cracking VI - Preparation and Characterization of Catalysts, Proceedings of the 6th International Symposium in Fluid Cracking Catalysts (FCCs), Vol. 194* (Eds: M. L. Occelli), Elsevier, **2004**, pp. 139 – 164.

[43] R. F. Wormsbecher, W.-C. Cheng, R. H. Harding, *Prepr. Am. Chem. Soc. Div. Pet. Chem.* **1995**, *40*, 482 – 486.
[44] A. A. Lappas, L. Nalbandian, D. K. Iatridis, S. S. Voutetakis, I. A. Vasalos, *Catal. Today* **2001**, *65*, 233 – 240.
[45] Y. Mathieu, A. Corma, M. Echard, M. Bories, *Appl. Catal. A* **2014**, *469*, 451 – 465.
[46] C. G. Schroer, P. Boye, J. M. Feldkamp, J. Patommel, D. Samberg, A. Schropp, A. Schwab, S. Stephan, G. Falkenberg, G. Wellenreuther, N. Reimers, *Nucl. Instrum. Methods Phys. Res. Sect. A* **2010**, *616*, 93 – 97.
[47] C. G. Ryan, R. Kirkham, R. M. Hougha, G. Moorhead, D. P. Siddons, M. D. De Jonge, D. J. Patersone, G. De Geronimod, D. L. Howarde, J. S. Cleverley, *Nucl. Instrum. Methods Phys. Res. Sect. A* **2010**, *619*, 37 – 43.
[48] C. A. Schneider, W. S. Rasband, K. W. Eliceiri, *Nat. Methods* **2012**, *9*, 671 – 675.
[49] Y. Liu, F. Meirer, P. A. Williams, J. Wang, J. C. Andrews, P. Pianetta, *J. Synchrotron Radiat.* **2012**, *19*, 281 – 287.

Received: June 21, 2015
Published online on September 1, 2015

